
## Università degli Studi di Trieste

Dipartimento di Fisica


Tesi di Laurea Triennale in Fisica

# Time-resolved Raman measurements in the cuprate superconductor $Bi_2Sr_2CaCu_2O_{8+\delta}$

---

## Misure Raman risolte in tempo sul cuprato superconduttore $Bi_2Sr_2CaCu_2O_{8+\delta}$


Relatore:

**Prof. Daniele Fausti**

Candidata:

**Costanza Lincetto**

Correlatori:

**Dott.ssa Angela Montanaro**
**Dott. Enrico Maria Rigoni**



Anno Accademico 2021/2022

# Sommario

La superconduttività è un fenomeno caratteristico di alcuni materiali, nei quali la resistenza elettrica è nulla al di sotto di una temperatura detta critica, la quale è generalmente alcuni gradi superiore allo zero assoluto per i superconduttori convenzionali. Negli anni '50 la teoria BCS (dai fisici Bardeen-Cooper-Schrieffer) ne ha fornito la prima descrizione miscroscopica: lo stato superconduttivo è descritto come una supercorrente di coppie di Cooper, uno stato legato di due elettroni che interagiscono attraverso lo scambio di un fonone.

Negli anni '80 venne scoperta una nuova classe di materiali superconduttori, nei quali la temperatura critica sale a temperature superiori di quella di ebollizione dell'azoto. Nonostante si sia studiato a lungo tale fenomeno, il meccanismo di formazione delle coppie di Cooper a tali temperature non è ancora chiaro.

In questa tesi si approfondirà lo studio dei cuprati: delle ceramiche a base di composti di ossido di rame. Questi materiali allo stato drogato sono dei superconduttori la cui temperatura critica sale fino a 100K. La fase superconduttiva è caratterizzata dall'apertura di una gap energetica, che nei cuprati ha una simmetria *d-wave* nella prima zona di Brillouin. Sono quindi definite due direzioni anisotrope: lungo l'*antinodo* la gap assume valore massimo, lungo il *nodo* è nulla. Lo stato superconduttivo è influenzato da tale gap anisotropa perché l'energia richiesta per rompere una coppia di Cooper dipenderà dal momento dell'eccitazione che fornisce tale energia.

Lo studio di tale gap è fondamentale per capire i meccanismi microscopici che portano alla formazione delle coppie di Cooper. A questo proposito, la spettroscopia Raman è uno strumento importante. Negli esperimenti Raman elettronici, le eccitazioni elettroniche nei solidi sono studiate attraverso lo scattering anelastico della luce, che è descritto dal cosiddetto tensore Raman. I diversi elementi di tale tensore possono essere isolati selezionando opportunamente la polarizzazione della luce incidente e scatterata. Tale tecnica è già stata implementata negli anni '80 per lo studio della gap superconduttiva nei cuprati all'equilibrio [1].

Per effettuare uno studio dinamico, si deve realizzare una versione *risolta in tempo* della spettroscopia Raman. Un'altra tecnica risulta fondamentale per questo scopo: la tecnica del pump&probe, che prevede di eccitare il materiale attraverso un impulso intenso (pump) e di studiare il suo rilassamento attraverso altri impulsi più deboli (probe).

Lo scopo di questa tesi è stato quello di combinare lo scattering Raman elettronico con la tecnica del pump&probe.

Per prima cosa si è sviluppato un modello per il tensore Raman (al terzo ordine) che tenesse in considerazione anche l'azione del pump, e non solo del probe, come avviene per il modello al primo ordine. Tale modello permette di studiare le eccitazioni al nodo e all'antinodo in funzione della direzione di polarizzazione del pump e del probe.

Per testare tale modello si è quindi sviluppato un setup sperimentale che permettesse di controllare la temperatura, la polarizzazione del pump e del probe, il ritardo temporale tra l'impulso di pump e gli impulsi di probe, l'energia degli impulsi.

Le misure sono state prese per due campioni del cuprato $Bi_2Sr_2CaCu_2O_{8+\delta}$ (uno *optimally doped*, l'altro *underdoped*) in diverse regioni del diagramma di fase. Variando i diversi parametri si è testata la validità del modello al terzo ordine del tensore Raman.

Dai dati raccolti si può concludere che la birifrangenza è una proprietà peculiare della fase superconduttiva, infatti per temperature più alte della temperatura critica i segnali ottenuti sono o nulli o deboli e non presentano nessuna dipendenza dall'angolo di polarizzazione del probe.

Dai dati ottenuti in fase superconduttiva si può concludere che sia il modello al primo ordine sia quello al terzo ordine non descrivono complessivamente le misure. Il modello al primo ordine predice segnale per tutti gli angoli di polarizzazione del probe, ma in nessuna delle configurazioni studiate (variando il campione e la polarizzazione del pump) si è ottenuto segnale indipendentemente dalla polarizzazione del probe. Il modello al terzo ordine invece descrive solo le misure ottenute per il campione *underdoped* e la polarizzazione del pump parallela alla direzione nodale. Se questa è parallela all'asse antinodale il segnale è traslato di 45° rispetto a quanto predetto dal modello.

# Introduction

Superconductivity indicates a set of properties characteristic of specific materials in which electrical resistivity abruptly drops to zero under a critical temperature, that is generally few degrees above the absolute zero in conventional metallic superconductors. A microscopic description of superconductivity was provided by the Bardeen-Cooper-Schrieffer (BCS) theory in 1957, in which the superconducting state is described as a superfluid current of Cooper pairs, a bound state of two electrons interacting via the exchange of a phonon.

Later on, a new class of superconductors was discovered in 1980s, in which the superconducting state is reached at temperatures much higher than in conventional superconductors and usually above the boiling temperature of liquid nitrogen. Although 40 years have passed, the pairing mechanism in these materials is still unknown. In particular, the BCS theory cannot explain how Cooper pairs are created at such higher temperatures.

In this thesis, we will focus on cuprates, a class of ceramic materials based on copper oxide compounds. These systems, upon hole- or electron-doping, show a rich phase diagram in which superconductivity can endure up to temperatures of 100K.

The superconducting phase is characterized by the opening of an energy gap at the Fermi energy. While in conventional superconductors the superconducting gap has a s-wave symmetry in the Brillouin zone, in cuprates the gap is characterized by a d-wave symmetry, which identifies two anisotropic directions in the Brillouin zone: along the *antinodal* direction the gap has maximum value, while it goes to zero along the *nodal* direction. This anisotropy in the gap energy influences the superconducting state because the energy required to break a Cooper pair into two quasiparticles (unpaired electrons) will depend on the momentum of the excitation that provides this energy.

The study of the anisotropy of the gap is instrumental to understand the microscopic mechanism that gives rise to electronic pairing in cuprates. This has stimulated in the past years the development of several momentum-resolved experimental techniques that enable the investigation of the nodal and antinodal contributions to the macroscopic superconductivity.

In this regard, Raman spectroscopy established as a powerful tool. In electronic Raman experiments, the electronic excitations in solids are studied through the inelastic scattering of light that is described by the so-called Raman tensor. By properly selecting the polarization of the incoming and the scattered light, different elements of the Raman tensor can be singled out and momentum-resolution can be achieved. This technique was implemented already in the late 1980s for the spectroscopic measurements of the d-wave gap in cuprates [1]. However, these measurements were performed at the equilibrium and cannot give any information about the dynamics of the Cooper pair breaking and recombination in momentum space.

In order to study the dynamics, a time-resolved version of Raman spectroscopy must be implemented. In this perspective, the pump-probe technique is pivotal. In a pump-probe experiment, the material is excited by a strong pulse (pump). Then its relaxation is probed by another weaker pulse (probe) that investigates how the optical properties of the sample

change during the relaxation time.

The aim of this thesis is to combine electronic Raman scattering experiments with a pump-probe scheme.

A first challenge of this approach is that its theoretical description cannot be entirely provided by the usual first-order Raman tensor, which takes into account only the interaction with one light beam (the probe). However, in a pump and probe experiment the action of the pump cannot be ignored. Here, we will develop a model that implements both the action of the pump and the probe in a third-order Raman tensor. We will rewrite this tensor considering the symmetries of the cuprates, that belong to the $D_{4h}$ group of the tetragonal lattice. This model allows us to study the nodal and antinodal excitations as function of the direction of the linear polarization of the pump and the probe.

In order to test this model, we will assemble an experimental setup that allows us to control all the freedom degrees we are interested in: temperature, pump and probe polarization, time delay between pump and probe pulses, photon energy of the pulses.

We perform measurements both in an underdoped and optimally doped sample of the cuprate $Bi_2Sr_2CaCu_2O_{8+\delta}$ in different regions of the phase diagram. By varying the experimental parameters, we test in which conditions the predictions of the third-order Raman tensor model are confirmed.

# Contents

# Chapter 1

# Fundamentals of superconductivity

In this chapter we will introduce the essential points to understand superconductivity, a phenomenon that was observed for the first time by Kammerlingh Onnes in 1911. We will describe firstly some experimental evidence about superconductors, then we will introduce the theoretical approach to conventional superconductivity.

We will focus on high temperature superconductivity and in particular on cuprates, like the samples that we have studied.

## 1.1 Superconductivity: phenomenological description

Superconductivity is a phenomenon that describes a phase of specific materials in which electrical resistivity drops suddenly to zero when these materials are cooled under a critical temperature $T_c$. This zero electrical resistivity explains the observation of a persistent electrical current, but can not describe the magnetic properties of these materials. In fact superconductors are perfect diamagnets. If a weak magnetic field is applied to a sample that we cooled below $T_c$, on the surface of the material there are electrical currents. These surface currents give rise to an other magnetic field that cancels the applied field inside the superconductor (figure 1.1). This is called the **Meissner effect**.

So inside the material we have $\boldsymbol{B} = 0$, a result that can not be derived simply from zero resistivity $\rho = 0$. In fact from Ohm's law, $\boldsymbol{E} = \rho \boldsymbol{j}$, if $\rho$ goes to zero and $\boldsymbol{j}$ is finite, then $\boldsymbol{E} = 0$. From Faraday's law, $\boldsymbol{\nabla} \times \boldsymbol{E} = -\partial_t \boldsymbol{B}$, we obtain $\partial_t \boldsymbol{B} = 0$, not $\boldsymbol{B} = 0$. So the Meissner effect suggests that perfect diamagnetism is a property characteristics of the superconducting state.

Considering a superconductor at temperature below $T_C$, an other parameter to control the superconducting state is the intensity of the applied field $B_a$. In fact, the application

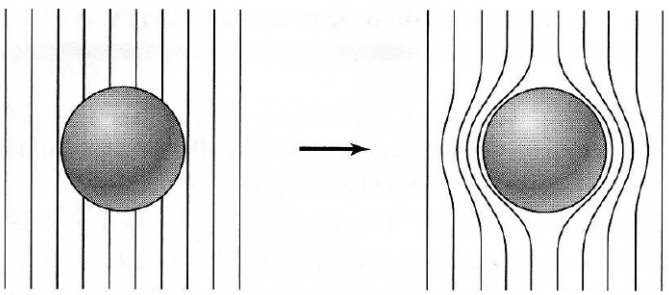

Figure 1.1: **Meissner effect.** When a superconducting sphere is cooled down in a constant magnetic field, passing the transition temperature $T_c$ the lines of the magnetic field are expelled from the inside of the sphere.[4]

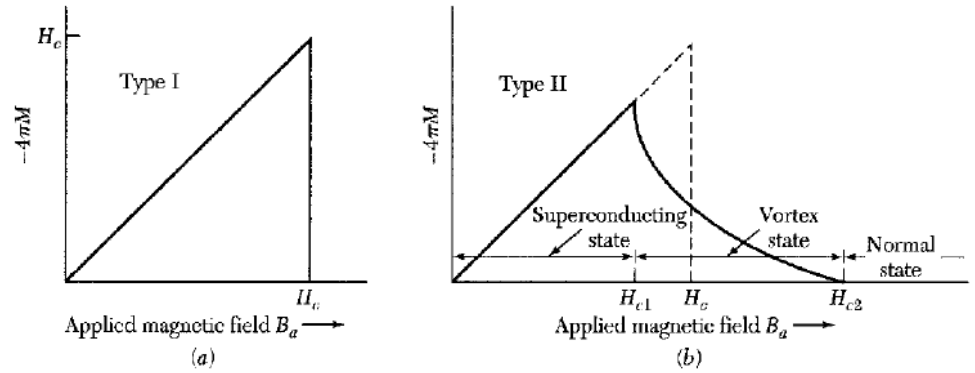


Figure 1.2: (a) **Superconductors of type I**: Under the critical field $H_c$ they are perfect diamagnets, above $H_c$ they are normal conductors. (b) **Superconductors of type II**: the flux begins to penetrate in the material at a field $H_{c1}$ and there is superconducting electrical properties up to $H_{c2}$. The state between $H_{c1}$ and $H_{c2}$ is called vortex state. Above $H_{c2}$ the sample is a normal conductor. On the vertical axes there is $-M$, the negative value correspond to diamagnetism. [4]

of a sufficiently strong magnetic field destroys the superconducting state. Therefore if the applied field is lower than a critical field $H_c$ the material is a perfect diamagnet, otherwise the applied field can penetrate the material. There are two types of superconductor that have different behaviour under the application of a field. The magnetization curve expected for superconductors of type I is sketched in figure 1.2 (a). Superconductors of type I, mostly pure samples of many materials, under $H_c$ are perfect diamagnets. Superconductors of type II have a magnetization curve like the one in figure 1.2 (b). These materials have superconducting electrical properties up to a critical field $H_{c2}$. Between the two critical fields $H_{c1}$ and $H_{c2}$ there is $B \neq 0$, we say that the Meissner effect is incomplete.

In normal metal the specific heat has the form $aT + bT^3$ at low temperature ($T$ for the electronic excitations, $T^3$ for the lattice vibrations). For temperature below the critical temperature $T_C$, the specific heat has higher values than in normal phases, then it slowly decreases. The explanation is that in superconducting state the linear electronic contribution is replaced by a term of the form $e^{\Delta/K_B T}$, that vanishes rapidly at low temperature. This is a characteristic behaviour of a system that has excited levels separated from the ground state by an energy $2\Delta$. This energy gap is centered about the Fermi energy $E_F$, so an electron of energy $E$ can be absorbed by (extracted from) the material only if $E - E_F$ ($E_F - E$) is greater than $\Delta$.

This energy gap has a different origin than the energy gap of insulators, in which it is caused by the electron-lattice interaction. In a superconductor we are interested in the electron-electron interaction.

### 1.1.1 London equation

The Meissner effect implies a magnetic susceptibility $\chi = -1$. We saw that put $\rho = 0$ in Ohm's law is not sufficient to explain this effect. We can modify Ohm's law in order to obtain the Meissner effect. In normal state we have $\boldsymbol{j} = \sigma \boldsymbol{E}$. In superconducting state we postulate that the current density is proportional to the vector potential of the local magnetic field:

$$\boldsymbol{j} = -\frac{1}{\mu_0 \lambda_L^2} \boldsymbol{A} \tag{1.1}$$

where $\lambda_L$ is a constant with the dimension of length. This equation is known as London equation, we can rewrite it considering $\boldsymbol{B} = \boldsymbol{\nabla} \times \boldsymbol{A}$:

$$\boldsymbol{\nabla} \times \boldsymbol{j} = -\frac{1}{\mu_0 \lambda_L^2} \boldsymbol{B}. \tag{1.2}$$

Under static conditions the Ampere-Maxwell law is $\boldsymbol{\nabla} \times \boldsymbol{B} = \mu_0 \boldsymbol{j}$, taking the curl of both sides and using equation 1.2 we obtain :

$$\nabla^2 \boldsymbol{B} = \frac{\boldsymbol{B}}{\lambda_L^2}. \tag{1.3}$$

This equation does not allow a solution uniform in space, in fact if we consider $\boldsymbol{B}(r) = \boldsymbol{B}_0 = costant$ we have that $\nabla^2 \boldsymbol{B} = 0$ always, so $\boldsymbol{B}_0$ is solution only if it is identically zero.

In a superconducting state the only solution allowed is a field exponentially damped as we go inside the material. If $B(0)$ is the field at the boundary and, for example, it is parallel to the boundary, the field inside is

$$B(x) = B(0) e^{-x/\lambda_L}, \tag{1.4}$$

where the expression for $\lambda_L$ is

$$\lambda_L = \left( \frac{\epsilon_0 m c^2}{n q^2} \right)^{1/2} \tag{1.5}$$

for particles with mass $m$, concentration $n$ and charge $q$. $\lambda_L$ is called London penetration depth, it measures the depth of penetration of the magnetic field. So an applied magnetic field will penetrate a sample only within a thickness much less than $\lambda_L$. This equation explains the macroscopic Meissner effect, but it can not describe the electrodynamics relate to a superconducting state.

### 1.1.2 About BCS theory

The basis of a quantum theory of superconductivity was laid by Bardeen, Cooper and Schrieffer in 1957.

The theory requires a net attractive interaction between electrons near the Fermi surface. This is possible thanks to the lattice-electron interaction: when one electron interacts with the lattice the result is a deformation of the lattice, then a second electron sees the deformed lattice and tends to lower its energy. So the second electron interacts with the first one via the deformation of the lattice, i.e. a phonon (for a representation of this interaction see figure 1.3). This attractive interaction is possible between electrons with energies sufficiently close together. The fact that a bound state is created through this weak interaction is possible thanks to the influence on the interacting pairing of the remaining $N - 2$ electrons, because of the Pauli exclusion principle.

Thanks to this attractive interaction between electrons there is a new ground state, that is superconducting and is separated by a finite energy $\Delta$ from the lowest excited state. The principal characteristics of the BCS ground state is that the orbitals are occupied by pairs, not by single particles. Therefore if an orbital with wavevector $\boldsymbol{k}$ and spin up $\uparrow$ is occupied (empty), also the one with $-\boldsymbol{k}$ and $\downarrow$ is occupied (empty). These pairs are called *Cooper pairs*.

The properties of these pairs, and also of the superconductivity that arises from them, are encoded in the pair wavefunction $\Phi_{\boldsymbol{k}}$, that is an s-wave function, so it is isotropic.

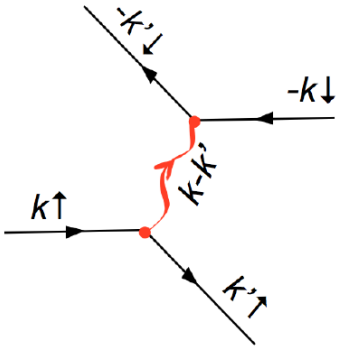


Figure 1.3: **Interaction between two electrons.** Considering the pair $(\boldsymbol{k}\uparrow, -\boldsymbol{k}\downarrow)$: the first electron scatters from $\boldsymbol{k}$ to $\boldsymbol{k'}$ creating a phonon with $\boldsymbol{k}-\boldsymbol{k'}$; the second electron scatters from $-\boldsymbol{k}$ to $-\boldsymbol{k'}$ absorbing the phonon. [6]

## 1.2 High temperature superconductivity

High temperature superconductivity (HTS) is characterized by a high transition temperature. The BCS theory can not explain how the mechanism of pairing works because at higher temperatures there are higher energies incompatible with the weak attractive energy between the two electrons of the pairs.

In this thesis we will examine cuprates, copper oxides high temperature superconductors.The superconductivity in cuprates was observed for the first time by Bednorz and Muller in 1986, still today the electronic pairing mechanism in these materials is not understood.

### 1.2.1 Cuprates

Cuprates are composed of copper oxide layers that are separated by other insulating planes of various chemical composition that act as charge reservoirs. In the copper oxide layers each copper ion is fourfold coordinated to the oxygen ions. The superconducting behaviour accurs in these $CuO_2$ planes.

The macroscopic properties of cuprates depend on the electronic structure of the $CuO_2$ plane. In the undoped material each Cu atom loses $2e^-$ because of the high electronegativity of the oxygen, so it is left in the $3d^9$ configuration.

Cuprates at pure state are insulating and antiferromagnetic, in order to see superconductivity we have to dope them. Through a p-doping we can substitute the cations of the insulating layers with other cations of minor valency. The consequence is a major presence of moving holes in the oxygen orbitals. The superconducting behaviour is connected to the presence of these holes.

A phase diagram as function of the temperature and the doping (p, that indicates the concentration of the holes) is represented in figure 1.4. In the area enclosed by the red line the cuprates have superconducting behavior. The critical temperature $T_C$ that denotes the superconducting (SC) phase is maximum at the optimal doping (OP, $p \sim 0.16$) and it decreases for underdoped (UD) and overdoped (OD) samples. For underdoped and optimally doped cuprates below $T^*$ there is a phase, called pseudogap phase (PG), that has peculiar symmetries and properties not yet well understood. In fact these properties are not characteristics neither of the SC phase nor the metallic one. Other phases occur in the phase diagram, we only mention them: for low dopings ($p < 0.05$) cuprates are insulating and antiferromagnetics, at high temperatures they are strange metals and for high dopings there is the Fermi liquid phase.

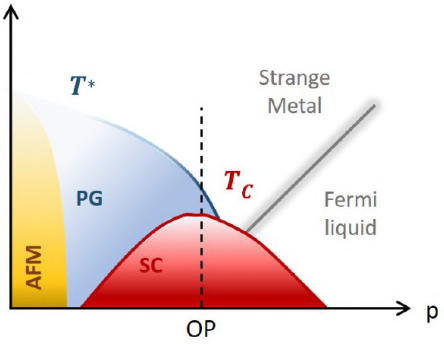


Figure 1.4: **Phase diagram of cuprates.** At very low dopings the cuprates are antiferromagnetics (yellow area). For the doping increases we have the superconducting phase under the critical temperature $T_C$ (red area), that is maximum at optimal doping. in the underdoped region and below $T^*$ there is the pseudogap phase (blue area), whose boundaries are uncertain at low dopings. Above $T^*$ cuprates are strange metals and increasing the doping there is a transition to the Fermi liquid phase. [2]

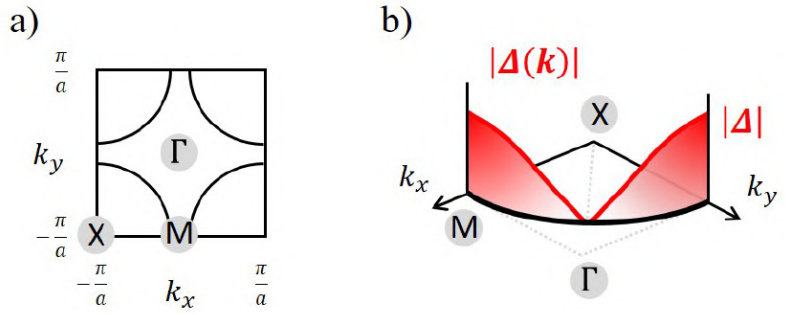


Figure 1.5: **d-wave superconducting gap in cuprates.** a) Fermi surface in the first Brillouin zone. b) Amplitude of the d-wave gap in the reciprocal space. [2]

We already said that in BCS theory the consequence of the Cooper pairing is a s-wave gap, that is isotropic across the first Brillouin zone. Instead in cuprates the gap has a strong momentum dependence that is consistent with a d-wave simmetry. The gap has maximum value along $\Gamma M$ axis (antinodal) and goes to zero along $\Gamma X$ axis (nodal), as shown in figure 1.5. This anisotropy influences the superconducting state because the energy required to break a Cooper pair into two quasiparticles (QP) depends on its momentum. Superconducting electrons are strongly bond for $\boldsymbol{k}$ parallel to the CuO bond, and they are not paired for $\boldsymbol{k}$ along CuCu direction. The consequence is that at the antinode electronics transitions are permitted only if the provided energy is bigger than the SC gap, at the node all transitions are allowed.

# Chapter 2

# Experimental techniques

In this chapter we will introduce the experimental techniques used. We will describe the pump-probe spectroscopy that allows to perform time-resolved measurements to study electron dynamics. Then we will describe Raman spectroscopy, that permits to study the excitations in solids through the inelastic scattering of light.

## 2.1 Pump-probe spectroscopy

Pump-probe experiments allow to study the evolution of optical properties of the sample during the relaxation time on a sub-picosecond timescale.

The material is excited trough a strong ultrafast laser pulse (pump), that drives the sample to a non-equilibrium state. Then its relaxation is controlled with other weaker laser pulses (probe), that are properly delayed in time with respect to the pump. These probe pulses measures the change of the transmission or the reflectivity of the samples as function of the time-delay between the pump and probe (figure 2.1). This delay is controlled varying the optical path of the probe. The electron dynamics we study have characteristic time of femstoseconds, therefore we need that the time delay between pump and probe pulses have this duration. In order to do this we need to be able to change the optical path in the range of micrometers. In fact to a time delay of 10fs correspond a change in the optical path of $3\mu$m.

It is important that the probe has an intensity minor than the pump in order to not perturb the system under study, in fact the probe only investigates optical properties of the sample.

The temporal resolution of the experiment is determined by the duration of the pulses. The development of ultrafast sources (that produces pulses which duration is less than picoseconds), allows to study processes like the electron relaxation.

### 2.1.1 Photoinduced dynamics in superconductors: Rothwarf-Taylor equations

The reflectivity of the material is proportional to the density of unpair electrons, so we need a model to describe how this concentration changes during the relaxation time. For this purpose we will consider the Rothwarf-Taylor model. The lifetime of these unpair electrons does not depend only by the recombination rate to reassemble the Cooper pairs, we need to consider also the phonon reabsorption process from ground state. We can summarize the process of relaxation of photoexcited electrons as follows (figure 2.2). Pump pulse excites the SC state breaking Cooper pairs releasing quasi-particles QPs (i.e. unpair electrons), then QPs recombine into pairs. They relax to the ground state if they emit a phonon with

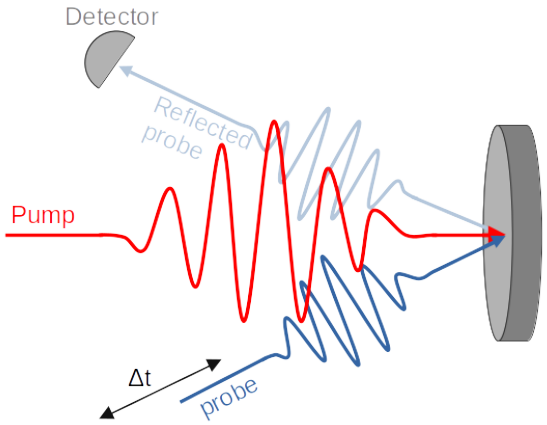


Figure 2.1: **Pump&probe technique**: The pump pulse excites the material, the probe pulses, changing their time delay with the pump, control the relaxation time through the variation of the reflectivity of the sample.

energy $\hbar\omega > 2\Delta$. The pairs at the ground state can break if they absorbe these phonons with high frequency. Therefore there is a cyclical process of breaking and recombination of Cooper pairs. This process end (and the superconductive state is re-established) when photoexcited particles reach states with energy near the gap, in particular it is terminated when a phonon decay with energy $\hbar\omega < 2\Delta$. The equations that describe this model are:

$$\begin{aligned} \frac{dn}{dt} &= I_0 + \eta N - Rn^2 \\ \frac{dN}{dt} &= -\frac{\eta N}{2} + \frac{Rn^2}{2} - \gamma(N - N_T). \end{aligned} \tag{2.1}$$

n is the population of QPs; N is the population of high frequency phonons, it is $N = N_{PE} + N_T$, where $N_{PE}$ indicates the photoexcited contributions and $N_T$ the thermal. $\eta$ is the probability for pair breaking by the absorption of a phonon; R is the QP recombination rate with the emission of a phonon; $I_0$ desribes the incident pulse. $\gamma$ describes the loss of phonons because of the decay of high frequency phonons ($\hbar\omega > 2\Delta$) into phonons of lower frequency ($\hbar\omega < 2\Delta$). The factor 2 comes from the fact that two QPs are recombined with an emission of a single phonon.

## 2.2 Electronic Raman scattering

In this section we will describe the fundamentals of Raman spectroscopy, a technique that allows to study excitations in solids through inelastically scattering of light. We will employ quantum mechanics formalism to give a deep insight on the problem [2]. In particular we will focus on Raman scattering on cuprates, superconductors that we introduced in the previous chapter, and how to study the d-wave superconducting gap thanks to time-resolved Raman measurements.

The physicist C.V. Raman in the 1920s observed that a little part of photons (around 1 over $10^8$) scatters inelastically, instead of elastically when light hits a solid. In particular this inelastically scattering can originated from the coupling of light to electrons (or also other excitations). Thanks to electronic Raman scattering we can study the electron dynamics described in the previous chapter and how they differ in different regions of the Brillouin zone. This is possible selecting the polarizations of the incoming and scattered photons.

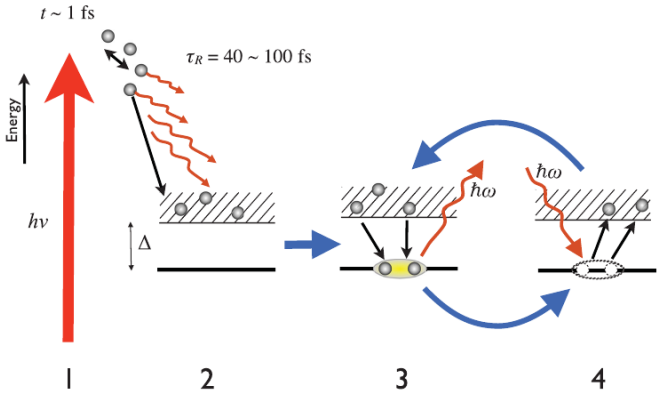


Figure 2.2: **Diagram of the relaxation of photoexcited electrons.** (1) Photoexcitations and creations of unpair electrons, (2) QPs recombine into pairs across the superconductive gap $\Delta$ through (3) emission of high frequency phonons ($\hbar\omega > 2\Delta$), (4) these phonons can break pairs leading to a cyclical process (blue arrows). When a high frequency phonons decay with energy $\hbar\omega < 2\Delta$ this process is terminated. [3]

### 2.2.1 Quantum mechanics description

In quantum mechanics Raman scattering can be interpretated as the creation or the annihilation of an elementary excitation in a solid. The mechanism of Raman scattering can be described as follows: the incoming light with wavevector $k_i$ and frequency $\omega_i$ interacts with the electronic system of the material, from the absorption of a photon there is a creation of an electron-hole pair that brings the system into a virtual state; this pair moves to an other state creating an elementary excitation with wavevector $q$ and frequency $\omega$; finally the electron and the hole recombine emitting a scattered photon with $k_s$ and $\omega_s$ (figure 2.3).

Now we will consider the Hamiltonian of N electrons with mass $m$, charge $e$ and momentum $p$ interacting with an electromagnetic field described trough the vector potential $\hat{A}(r_i)$:

$$H = \sum_{i=1}^{N} \frac{\left[\hat{p}_i + (e/c)\hat{A}(r_i)\right]^2}{2m} + H_C + H_F, \tag{2.2}$$

where $H_C$ is the Hamiltonian of the Coulomb interaction between electrons and $H_F$ is the Hamiltonian of the free electric field. By expanding the kinetic term we obtain:

$$\begin{aligned} H &= \frac{1}{2m}\sum_i \hat{p}^2 + \frac{e}{2mc}\sum_i \left[\hat{p}_i \cdot \hat{A}(r_i) + \hat{A}(r_i)\cdot \hat{p}_i\right] + \frac{e^2}{2mc^2}\sum_i \hat{A}^2(r_i) + H_C + H_F \\ &= \tilde{H} + H'_{int} + H''_{int}, \end{aligned} \tag{2.3}$$

where $\tilde{H} = H_0 + H_F$; $H_0 = \frac{1}{2m}\sum_i \hat{p}^2 + H_C$ is the Hamiltonian that describes the material, with eingestates defined by $\hat{H}_0 |\alpha\rangle = E_\alpha |\alpha\rangle$, that are labelled by the band index, spin and orbital quantum numbers.

In electronic Raman scattering the observable is the total cross section for scattering from electrons illuminated by the incident light. The cross section is the probability that an incoming photon with momentum $q_i$, frequency $\omega_i$ and polarization $e_q^{(i)}$ is scattered within a solid angle interval $(\Omega, \Omega + d\Omega)$ and an energy interval $(\omega_s, \omega_s + d\omega_s)$. We will consider the differential cross section that we can write through the Fermi's golden rule:

$$\frac{\partial^2\sigma}{\partial\Omega\partial\omega_s} \propto \frac{\omega_s}{\omega_i}\frac{1}{Z}\sum_{I,F} e^{-E_I/k_BT}|M_{F,I}|^2\delta(E_F - E_I - \hbar(\omega_i - \omega_s)), \tag{2.4}$$

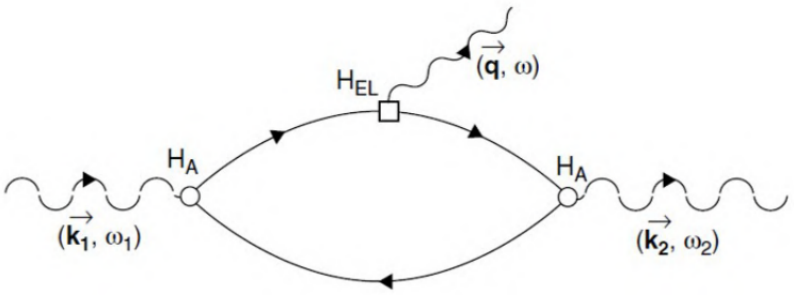


Figure 2.3: **Feynman diagram of a one-phonon Raman scattering**: $k_{1,2}$ and $\omega_{1,2}$ are the wavevectors and frequency of incoming and scattered photons respectively,; $q$ and $\omega$ are those of the elementary excitation created. $H_A$ represent the electron interaction with the field, $H_{EL}$ with the lattice. [7]

where $k_B$ is the Boltzmann costant, $I$ and $F$ indicate the initial and final state of the electronic system with energy $E_I$ and $E_F$. $\frac{1}{Z}\sum_{I,F} e^{-E_I/k_BT}$ is the probability to have the system in the $j^{th}$ microstate. $|M_{F,I}|^2$ is the matrix element that determine the light scattering:

$$|M_{F,I}|^2 = \langle F; q_s, w_s, e_q^{(s)}|H'_{int} + H''_{int}|I; q_i, w_i, e_q^{(i)}\rangle\,, \tag{2.5}$$

where $H'_{int}$ couples the electron's current with a photon, $H''_{int}$ couples the electron's charge with two photons.

### 2.2.2 Raman scattering in cuprates

We can simplify the computation of the matrix element $M_{F,I}$ considering the symmetries of the material, in fact the density fluctuations of the charge are modulated along the polarization direction of incident and scattered photons. The elements of the Raman matrix are non-zero only when then system (including incident and scattered photonos, Raman excitation) is even under the symmetry operations that are characteristics of the crystal symmetries. So we can consider basis functions of the irreducible point group of the crystal $\phi_\mu$ in order to decomposed the Ramam matrix element:

$$M_{F,I} \to \sum_\mu M_\mu \phi_\mu. \tag{2.6}$$

We will use the Mullikan notation:

- A (B): symmetric (anti-symmetric) with respect to rotation about the principal axis;
- 1 (2): symmetric (anti-symmetric) with respect to plane reflection orthogonal to the principal axis;
- g (u): symmetric (anti-symmetric) with respect to inversion trough the center.

Most cuprates belong to the $D_{4h}$ group of the tetragonal lattice. The modes can be odd (u-ungerade) or even (g-gerade) if they change or not sign upon inversion. In order to rewrite the Raman matrix element we will consider $R_\mu$ that are operators projected in the $\mu$ representation:

$$\begin{aligned} M_{F,I} =& \frac{1}{2}[R^{(1)}_{A_{1g}}(e_i^x e_s^x + e_i^y e_s^y) + R^{(2)}_{A_{1g}}(e_i^z e_s^z) + \\ &+ R_{B_{1g}}(e_i^x e_s^x - e_i^y e_s^y) + R_{B_{2g}}(e_i^x e_s^y + e_i^y e_s^x) + \\ &+ R_{A_{2g}}(e_i^x e_s^y - e_i^y e_s^x) + R^{(1)}_{E_g}(e_i^x e_s^z + e_i^z e_s^x) + R^{(2)}_{E_g}(e_i^y e_s^z + e_i^z e_s^y)], \end{aligned} \tag{2.7}$$

$e^{\alpha}_{i,s}$ indicate the polarization of the incident and scattered photons. In general we can not measured individually the different irreducible representations with polarizations in the $x-y$ plane in the $D_{4h}$ crystals. For example, if both incident and scattered photons are polarized along $\hat{x}$, the matrix element would be:

$$M_{F_I} = \frac{1}{2}[R^{(1)}_{A_{1g}}(e^x_i e^x_s) + R_{B_{1g}}(e^x_i e^x_s)], \tag{2.8}$$

so modes $A_{1g}$ and $B_{1g}$ are simultaneously measured.

We consider incoming light perpendicular to the $CuO_2$ plane, so it has not z-component, and we work with linear polarized light, therefore from equation 2.7 we can ignore modes $E_g$ (that could be seen if the incoming light is polarized along $\hat{z}$) and $A_{2g}$ (that could be seen only with circular polarized light). So we can consider only modes $A_{1g}$, $B_{1g}$ and $B_{2g}$ that can be re-written respectively in the following form:

$$\begin{pmatrix} a & & \\ & a & \\ & & b \end{pmatrix} \begin{pmatrix} c & & \\ & -c & \\ & & \end{pmatrix} \begin{pmatrix} & & d \\ & & \\ -d & & \end{pmatrix}, \tag{2.9}$$

where the first matrix represents the $A_{1g}$ mode, the second $B_{1g}$ and the third $A_{2g}$. So the Raman matrix element for our configuration is:

$$M_{F_I} = \frac{1}{2}\begin{pmatrix} R_{A_{1g}} + R_{B_{1g}} & R_{B_{2g}} \\ R_{B_{2g}} & R_{A_{1g}} - R_{B_{1g}} \end{pmatrix} \tag{2.10}$$

From now on we will set the x-axis along the CuO bond. Now the purpose is to isolate $B_{1g}$ and $B_{2g}$ modes: in order to do this we impinge on the samples with photons polarized along CuCu bond and CuO bond.

In order to study the $\boldsymbol{k}$-projections of the $A$ and $B$ modes, it is useful to write their basis functions $\phi_\mu(k)$ taken from the complete set of the Brillouin zone (BZ) harmonics for the $D_{4h}$ space group:

$$\begin{aligned} A_{1g} &\longrightarrow \frac{1}{2}\left(\cos(k_x a) + \cos(k_y a)\right) \\ B_{1g} &\longrightarrow \frac{1}{2}\left(\cos(k_x a) - \cos(k_y a)\right) \\ B_{2g} &\longrightarrow \sin(k_x a)\sin(k_y a) \end{aligned} \tag{2.11}$$

Each modes corresponds to a different projection in the BZ zone. From figure 2.4 we can see that $A_{1g}$ mode is total-symmetric, instead $B_{1g}$ and $B_{2g}$ are sensitive to specific directions in the reciprocal space: scattered light couples to charge excitations along the axes of the BZ ($k_{x,y} = 0$) for $B_{1g}$ symmetry, while it couples to excitations along BZ diagonals ($k_x = \pm k_y$) for $B_{2g}$ symmetry. In particular, given the d-wave symmetry of the SC gap (as discussed in the previous chapter), the $B_{1g}$ mode probes the antinodes of the gap, while the $B_{2g}$ mode probes the nodal regions.

Now we introduce the angles $\phi$ and $\alpha$ that indicates the polarization of the incoming probe and of the reflected beam. The action of the probe and the analyzer can be respectively written:

$$|p\rangle = \begin{pmatrix} \cos(\phi) \\ \sin(\phi) \end{pmatrix}, |A\rangle = \begin{pmatrix} \cos(\alpha) \\ \sin(\alpha) \end{pmatrix}, \tag{2.12}$$

these states are used to comput the Raman element, starting from the tensor:

$$M_{FI} = \begin{pmatrix} a + c & d \\ d & a - c \end{pmatrix}. \tag{2.13}$$

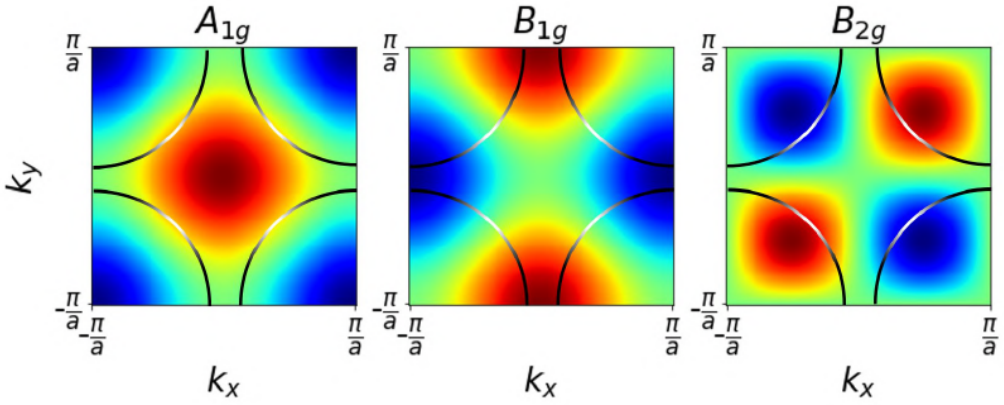


Figure 2.4: **Momentum-dependent sensitivity of Raman modes.** The curved lines are the Fermi surface, the color gradient indicates the amplitude of the d-wave gap: black at the antinodes and white at the nodes. [2]

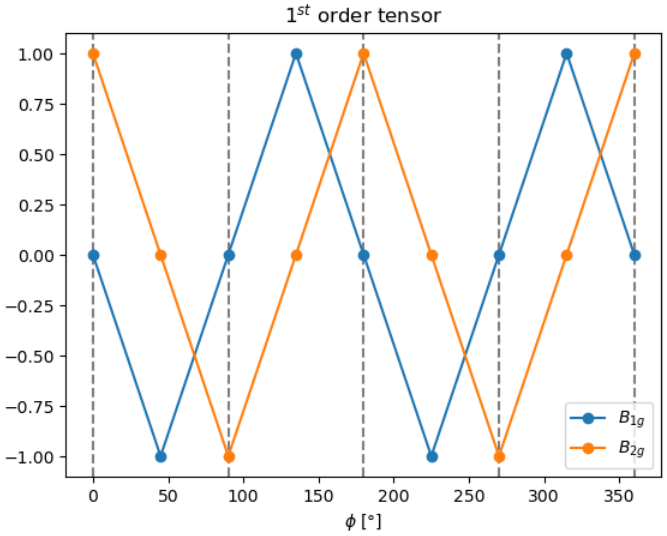


Figure 2.5: **First order model.** Model prediction for equation 2.14. The grey vertical lines indicate the $CuO$ axes.

In order to obtain the polarization-dependent contribution of each mode:

$$\begin{aligned}\langle A|M_{FI}|p\rangle &= (\cos(\alpha)\sin(\alpha))\begin{pmatrix} a+c & d \\ d & a-c\end{pmatrix}\begin{pmatrix}\cos(\phi)\\ \sin(\phi)\end{pmatrix} \\ &= A_{1g}\cos(\phi-\alpha) + B_{1g}\cos(\phi+\alpha) + B_{2g}\sin(\phi+\alpha) \\ &= A_{1g}\cos(\mp 45^\circ) + B_{1g}\cos(2\phi \pm 45^\circ) + B_{2g}\sin(2\phi \pm 45^\circ),\end{aligned}$$

where in the last equivalence we used that in our configuration $\alpha = \phi \pm 45^\circ$; we make the difference between the two contributes and obtain:

$$\Delta R_+ - \Delta R_- \propto B_{2g}\cos(2\phi) - B_{1g}\sin(2\phi). \tag{2.14}$$

We obtained a model that describe the $D_{4h}$ symmetry at first order, ignoring the action of the pump (figure 2.5). If $\phi = 0 + k\pi/2$ the signal measured is proportional to $\pm B_{2g}$, and, analogously, it is proportional to $\pm B_{1g}$ if $\phi = \pi/4 + k\pi/2$.

### 2.2.3 Third-order Raman tensor

In a pump-probe experiment we have to consider also the action of the pump, this can be done through the third order Raman tensor:

$$R^{(3)}_{ijkl} = R^{ij}_{A_{1g}} R^{kl}_{A_{1g}} + R^{ij}_{B_{1g}} R^{kl}_{B_{1g}} + R^{ij}_{B_{2g}} R^{kl}_{B_{2g}}$$

$$= \begin{pmatrix} \begin{pmatrix} a^2+c^2 & 0 \\ 0 & a^2-c^2 \end{pmatrix} & \begin{pmatrix} 0 & d^2 \\ d^2 & 0 \end{pmatrix} \\ \begin{pmatrix} 0 & d^2 \\ d^2 & 0 \end{pmatrix} & \begin{pmatrix} a^2-c^2 & 0 \\ 0 & a^2+c^2 \end{pmatrix} \end{pmatrix} \tag{2.15}$$

where the indices $i, j, k, l = 1, 2$, the first two indices indicate the pump polarization, the other two the polarization of incoming and scattered beam.

We will consider $\phi$ and $\alpha$ as above and we introduce also $\theta$ to indicate the polarization of the pump, which action is represented by

$$|P\rangle = \begin{pmatrix} \cos\theta & 0 \\ 0 & \cos\theta \\ \sin\theta & 0 \\ 0 & \sin\theta \end{pmatrix}.$$

Starting from the action of the pump we get:

$$R^{(pump)} = \langle P | R^{(3)}_{ijkl} | P \rangle = \begin{pmatrix} a^2 + c^2\cos(2\theta) & d^2\sin(2\theta) \\ d^2\sin(2\theta) & a^2 - c^2\cos(2\theta) \end{pmatrix}$$

then from the action of the probe we get:

$$R^{(probe)} = R^{(pump)} |p\rangle = \begin{pmatrix} (a^2 + c^2\cos(2\theta))\cos\phi + d^2\sin(2\theta)\sin\phi \\ d^2\sin(2\theta)\cos\phi + (a^2 - c^2\cos(2\theta))\sin\phi \end{pmatrix}$$

at last the action of the analyzer:

$$\Delta R = \langle A | R^{(probe)} = a^2\cos(\phi - \alpha) + c^2\cos(2\theta)\cos(\phi + \alpha) + d^2\sin(2\theta)\sin(\phi + \alpha).$$

With reference to the relations in 2.9, we can write:

$$\Delta R(\theta, \phi, \alpha) = A_{1g}\cos(\phi - \alpha) + B_{1g}\cos(2\theta)\cos(\phi + \alpha) + B_{2g}\sin(2\theta)\sin(\phi + \alpha),$$

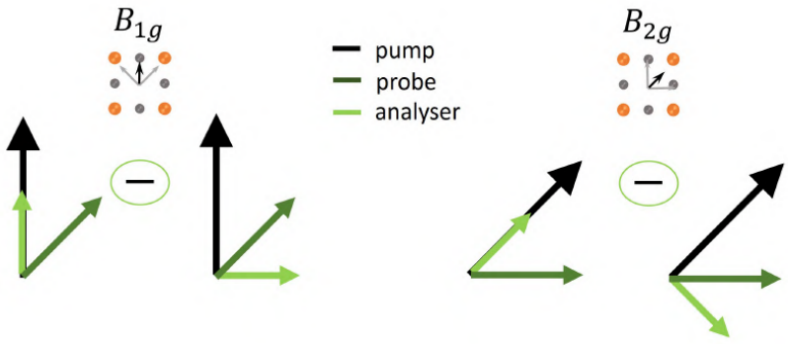


Figure 2.6: **Birefringence measurements of the B1g and B2g modes.** We select the orthogonal projections (analyser) of the probe, then we evaluate their difference. The orange (grey) circles are ions of $Cu^{2+}$ ($O^{2-}$).

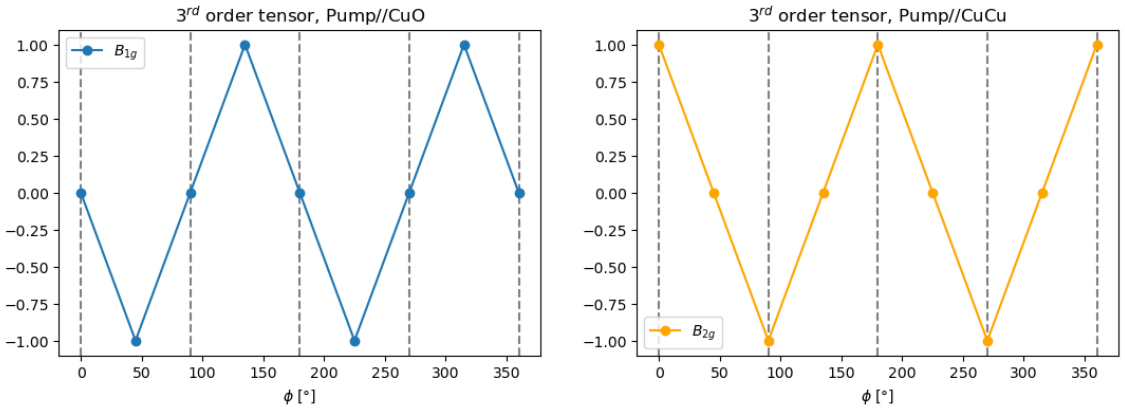


Figure 2.7: **Third order model.** Model predictions for the $B_{1g}$ mode (equation 2.17, $\theta = 0°$) and the $B_{2g}$ model (equation 2.18, $\theta = 45°$). The grey vertical lines indicate the $CuO$ axes.

where in our configuration we select the orthogonal projections through a polarizing beam splitter, so $\alpha = \phi \pm 45°$, and we can re-write:

$$\Delta R(\theta, \phi, \alpha) = A_{1g}\cos(\mp 45°) + B_{1g}\cos(2\theta)\cos(2\phi \pm 45°) + B_{2g}\sin(2\theta)\sin(2\phi \pm 45°),$$

but we are interested in the difference between the two projections (figure 2.6):

$$\Delta R_{+/-} = \Delta R_{+} - \Delta R_{-} \propto B_{2g}\sin(2\theta)\cos(2\phi) - B_{1g}\cos(2\theta)\sin(2\phi). \tag{2.16}$$

If we put $\theta = 0$, that is polarization of the pump parallel to the CuO bond, $B_{1g}$ can be isolated:

$$\Delta R_{+/-} \propto B_{1g}\sin(2\phi), \tag{2.17}$$

instead with $\theta = 45°$, pump parallel to CuCu bond, $B_{2g}$ can be isolated:

$$\Delta R_{+/-} \propto B_{2g}\cos(2\phi). \tag{2.18}$$

So including the action of the pump in the model, we can isolate the $B_{1g}$ and $B_{2g}$ modes separately (figure 2.7). If the pump polarization is parallel to the $CuO$ bond ($\theta = 0°$) the $B_{1g}$ is isolated, and we expect signal for $\phi = \pi/4 + k\pi/2$, when the probe is parallel to the $CuCu$ bond. Instead if the pump is parallel to $CuCu$ ($\theta = 45°$) we isolate the $B_{2g}$ mode, we expect signal for $\phi = 0 + k\pi/2$, when the probe is parallel to $CuO$ bond.

# Chapter 3

# Experimental setup

In this chapter we will describe the experimental setup developed in order to study time-resolved electronic Raman scattering in cuprates. We will describe all the components necessary to perform a pump-probe experiment as explained in chapter two.

Then we will briefly give a description of the samples used.

## 3.1 Setup

The main components of the set up are described in figure 3.1. We use a commercial laser light source (Pharos, Light conversion) to generate ultrashort pulses (with central wavelength of 1030nm and duration of 200fs) with a repetion rate of 50kHz (but we will work with a repetion rate of 5kHz, selecting one pulse over ten). In order to obtain pulses at tunable wavelengths, we use instruments that exploit non linear optical processes, like the photon down conversion process, as Optical Parametric Amplification (OPA) and Difference Frequency Generation (DFG).

In particular we obtain the probe pulses with a non-collinear OPA (NOPA), that allows to obtain broadband pulses shorter than 25fs and with wavelength centered in 750nm (broadband probe pulses allow to study the response of the sample in a wide range of wavelengths). To obtain the mid-infrared pump pulse (17$\mu$m), we use Twin OPAs in combination with a DFG crystal.

The temporal delay between the probe and the pump beams is controlled by a motorized stage that modifies the optical path of the probe.

In order to isolate the modes of the sample by choice of a specific geometry, as we have explained in the section 2.2, we need to implement a setup that allows to select different angles for the linear polarization of the pump and the probe.

In front of the sample there is an half-waveplate $\phi$ that defines the polarization of the incoming probe. A second half-waveplate $\alpha$ is placed after the sample and before the polarizing beam splitter. We use it to realign the reflected beam with the polarization of the incoming probe. Then we split the beam in its orthogonal projections through the polarizing beam splitter. The two components are independently diffracted by two transmission gratings and focused into two linear arrays of silicon photodiodes. With reference to figure 3.1, detector Ch0 measures the vertically polarized component, while detector Ch1 the horizontal one.

The polarization of the pump is fixed vertical, so to measure different modes (that can be isolated stimulating the sample along CuCu or CuO bonds) we need to rotate the sample (figure 3.2). The orientation of the sample is controlled by a piezoelectric rotator.

In order to control the temperature of samples, these are inserted in a closed cycle liquid helium cryostat. The cryostat expander is supported by a custom made structure fixed to

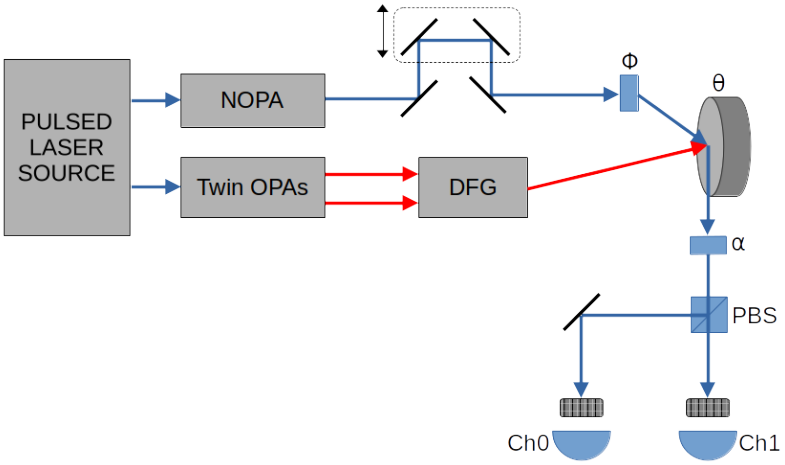


Figure 3.1: **Diagram of the experimental set-up:** the probe ($750nm$) is obtained in a non-collinear OPA, the mid-infrared pump through twin OPAs and a DFG crystal, the temporal overlap between probe and pump is controlled by a motorized stage. $\phi$ and $\alpha$ are two half-waveplates that allow to controll the polarization of the incoming and reflected probe, $\theta$ indicates the orientation of the sample that is controlled by an electric rotator. A polaryzing beam splitter (PBS) splits the reflected probe into two components that are dispersed by two transmissions gratings and the focused on two arrays of photodiodes.

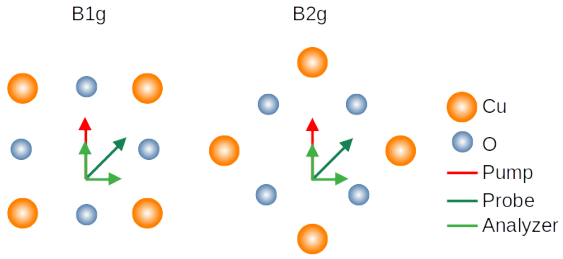


Figure 3.2: **Configuration of beam polarization and sample.** To select $B_{1g}$ and $B_{2g}$ modes we rotate the sample because the pump has fixed vertical polarization. Through a PBS we split the reflected probe into two components at $\pm 45°$ (analyzer) and detect them.

the laboratory floor and the cold head is fixed to the optical bench. This solution isolates the samples from the characteristic vibrations of the expander.

The samples are mounted on a copper plate that is connected to the cold head and also fixed to the moving part of a piezo-electric rotator. A thermocouple is placed on the copper plate, in proximity of the samples. It is used to measure the sample temperature. In order to improve the conductivity of this structure, indium foils are interposed at each metallic interface. The minimum temperature we can reach for samples is $35K$, because of the piezoelectric rotator and the not perfect conductivity.

The entire structure is enclosed in a vacuum chamber that is provided with a 1-inch window that allows optical access. Vacuum conditions are matched via a standard turbo pumping station that allows to reach pressures of $10^{-7}$mbar working at ambient temperature and pressures of $10^{-8}$mbar working at cryogenic temperature.

### 3.1.1 Array calibration

Everytime we adjust the optical alignment it is necessary to perform a wavelength calibration to establish a relation between the array pixel number and the wavelength of the light

component impinging on each pixel.

We use a filter with a known spectrum (thorlabs) and place it before the sample. This filter cuts the central frequencies of the pulses, obtaining a shape with two peaks that we use as reference points (the red line in figure 3.3). Once the filter is placed, we measure its spectrum first with an optical fiber spectrometer already calibrated, then with the arrays of our detection (figure 3.4). In this way we can assign the two peaks to a pixel number and to a specific wavelength. Through a linear interpolation (figure 3.5) we obtain the wavelength calibration of the arrays.

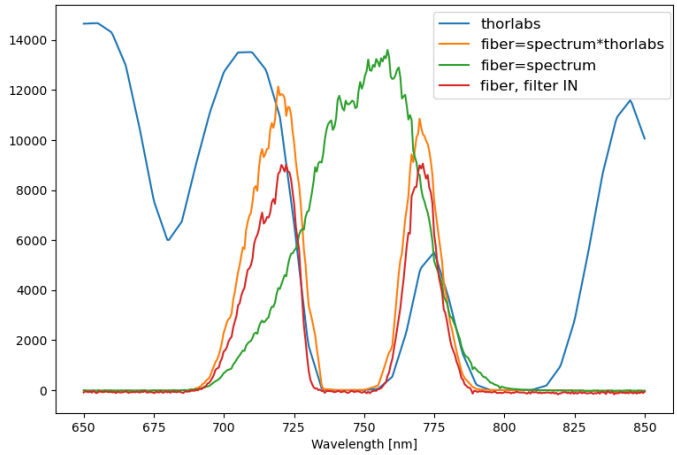


Figure 3.3: **Action of the thorlabs filter on the pulse spectrum.** The blue line is the transmission spectrum of the filter (thorlabs). The green line is the spectrum of the optical pulse measured by a calibrated optical fiber. Orange line is obtained by multiplying the filter curve (blue) for the pulse spectrum (green). It shows a good agreement with the spectrum measured when the filter is inserted in the optical path of the probe beam (red line).

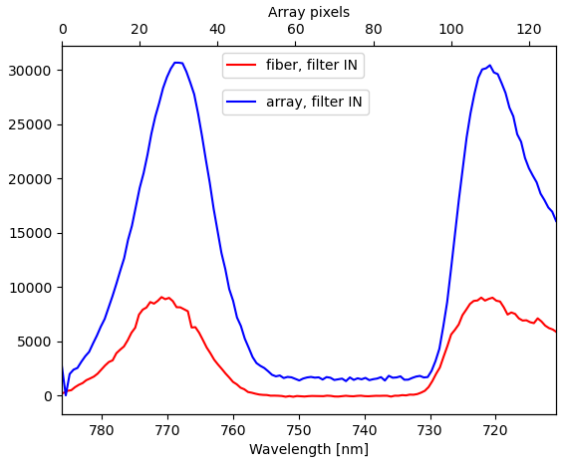


Figure 3.4: **Measurements of the pulse spectrum with the filter in.** The blue line is the spectrum filter measured with the photodiods arrays, the red one is measured with the optical fiber.

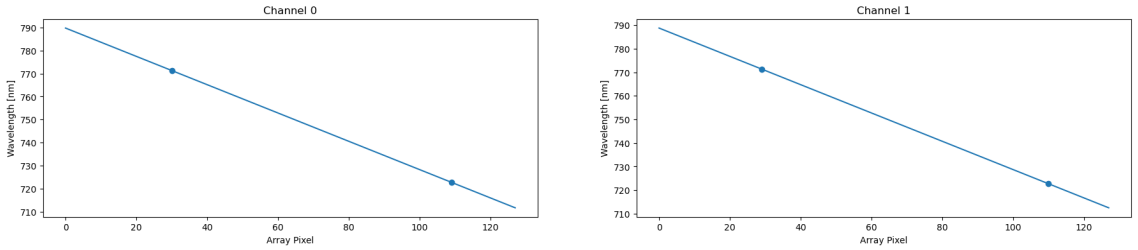


Figure 3.5: **Wavelength calibration of the arrays:** linear interpolation between the 128 pixels of the arrays and wavelengths.

### 3.1.2 Chopped detection

In order to do a pump and probe experiment we need to collect both the pumped and unpumped signals. To do this we use an optical chopper, a wheel that mechanically blocks the pump beams at the frequency of $45Hz$. As sketched in figure 3.6, we divide the train of probe pulses into two groups: N pumped pulses (those probe spectra reflected by the sample when the pump hit the sample) and N unpumped pulses (reflected when the pump was blocked by the chopper blade). In particular we measure the intensity of the $i^{th}$ reflected beams $R_i^{P,U}(\lambda, t)$ as function of its wavelength $\lambda$ and the time delay between the pump and the probe beams $t$.

In order to understand how the signals change depending on the presence or not of the excitation of the pump, we are interested in the difference between the pumped $R_i^P(\lambda, t)$ and unpumped $R_i^U(\lambda, t)$ signals. So the observable is the differential reflectivity normalized to the unpumped reflectivity:

$$\frac{\Delta R(\lambda, t)}{R} = \frac{\sum_{i=1}^{N} R_i^P(\lambda, t) - \sum_{i=1}^{N} R_i^U(\lambda, t)}{\sum_{i=1}^{N} R_i^U(\lambda, t)}. \tag{3.1}$$

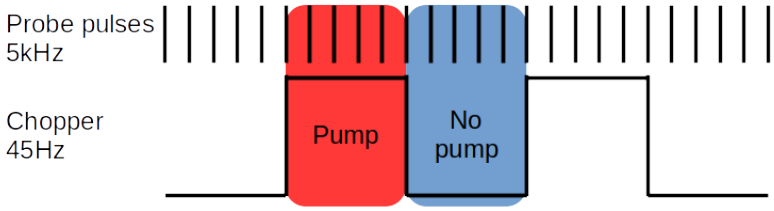


Figure 3.6: Acquisition of pumped and unpumped signals with the use of a chopper.

## 3.2 Description of the samples

We worked with two samples of the cuprate $Bi_2Sr_2CaCu_2O_{8+\delta}$ (or briefly Bi2212) with different doping: one optimally doped (OP) with critical temperature $T_C = 90K$ and one underdoped (UD) with $T_C = 80K$. In the OP sample the amplitude of the antinodal gap is of the order of 70meV.

These cuprates belong to the high critical temperature copper oxide based superconductors $Bi_2Sr_2Ca_{m-1}Cu_mO_{2m+4+\delta}$. $m$ indicates the number of $CuO_2$ planes in the unit cell of the material, so in the Bi2212 there are two-planes of $CuO_2$. $\delta$ indicates the doping level. In figure 3.7 we reported the crystal structure of the optimal doped Bi2212.

Referring to the phase diagram studied in the first chapter (figure 1.4) we see that these samples have three phases varying the temperature. They are superconductors under the

critical temperature $T_C$. For temperatures that go from $T_C$ to $T^*$ there is the pseudogap phase, that is wider for the underdoped sample. Above $T^*$ there is the normal phase.

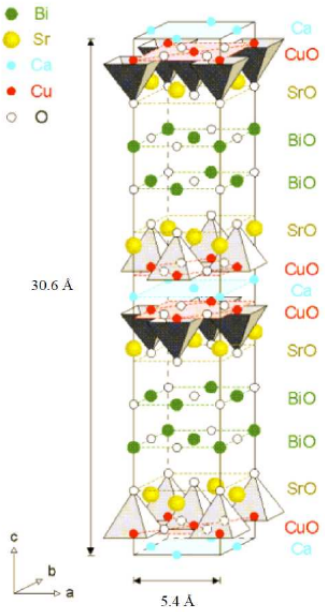


Figure 3.7: The unit cell of $Bi_2Sr_2CaCu_2O_{8+\delta}$ [8]

# Chapter 4

# Measurements and data analysis

In this chapter we will describe the measurements obtained, referring to the technique discussed in the second chapter.

We will consider the signals collected by the two detectors to study the transition between the three phases: superconducting, pseudogap and normal phases.

Then we will consider the birefringence map, obtained subtracting the single channel maps, to study the relaxation electron dynamics in the superconducting phase when the samples are excited by a pump of energy lower than the energy gap. We will compare the data collected with the models obtained in the second chapter. We will study first the underdoped sample, then the optimally doped sample. In order to excite along the nodal or antinodal direction we will rotate the samples themselves and we will study their reflectivity varying the angles of the probe pulses.

## 4.1 Reflectivity map

In the previous chapters we described the pump and probe technique and how to implement it in an experimental setup. In particular in chapter 3 we described the chopped detection that allows to distinguish pumped signals from the unpumped. The observable in our measurements is the differential reflectivity normalized $\Delta R/R(\lambda, t)$ in equation 3.1.

These maps depend on the reflectivity intensity (colormap), the wavelength of the reflected probe (vertical axis) and the time-delay between the pump and the probe (horizontal axis). At time t=0, the pump and the probe beams are temporally overlapped in the sample. Through the ultrashort probe pulses we can map the relaxation of the samples in a time range of 5ps.

The color gradient (figure 4.1a) indicates the reflectivity intensity. We have maximum signal at the overlap, that decreases for positive time. We have weaker signals for low wavelength. These features can be clearly addressed in figure 4.1b, where we presented the reflectivity signal only for few selected wavelengths. The transient signal is more pronounced in the wavelength range 760nm-790nm.

## 4.2 Temperature measurements

In order to estimate the critical temperature $T_C$ and the temperature $T^*$ that defines the pseudogap (PG) phase of our samples we performed a measurement varying continuously the temperature from 50K to 220K and acquiring a pump-probe trace at each temperature step. It is not possible to perform this measurement with a unique scan. In fact heating up the samples the optical alignment is lost because of the thermal expansion. Therefore we split the measurement into two temperature ranges: the first allows to identify $T_C$,

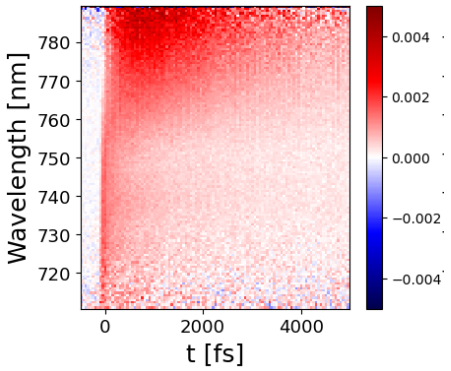


(a) **Reflectivity map:** the map corresponds to the signal $\Delta R/R$ detected by one array and integrated over the total number of pulses.

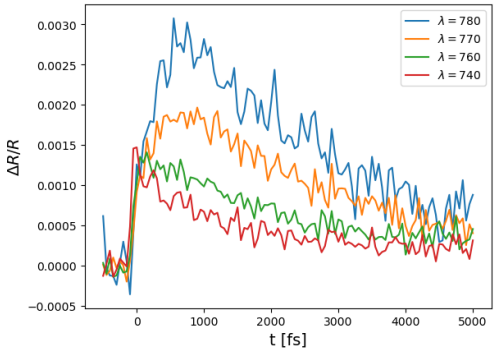


(b) **Dependence from the wavelength:** each line corresponds to horizontal cuts of the reflectivity map. Each line represents the time trace of the transient reflectivity signal with a specific wavelength.

Figure 4.1

the second $T^*$. In figure 4.2 the temperature maps display the transient reflectivity signal (integrated in the spectral region 777-783nm) as function of the time delay. These maps are measured on the samples at different temperatures: the solid lines mark the transition between the superconducting phase and the pseudogap phase (green) and the PG-normal phase transition (yellow).

Cooling down the temperature, $T^*$ is identified by the appearance of a negative signal in the $\Delta R/R$ map, $T_C$ when a positive signal appears. From figure 4.2a we can estimate that for the optimally doped sample $T^* \simeq 142K$ and $T_C \simeq 80K$. From figure 4.2b we obtain $T^* \simeq 200K$ and $T_C \simeq 73K$ for the underdoped sample. We highlight that the nominal value of the critical temperature for the OP and UD samples are respectively $90K$ and $80K$. The reason of this incongruity may be in the fact that we are heating the sample with the laser, whose repetition rate was set at $5kHz$ for the experiment. To test our assessment, we repeated the measurement with a lower repetition rate of the laser, 2kHz. Indeed repeating the temperature scan in the UD sample we see that $T_C$ is affected by the repetition rate (figure 4.3). For repetition rate of 5kHz we already obtained $T_C = 73K$, for 2kHz we see that the critical temperature increases nearly to 80K.

The effect of the repetition rate is important to understand where the SC and PG behaviours arises in our sample considering the action of the pulses. We are interested to make the measurements in the difference phases: to study the SC phase we cool the sample at $T \simeq 35 - 40K$, for the PG phase at $T \simeq 100K$. Doing the measurements with these temperature values we are sufficiently distant from the transition temperatures. So we can ignore the heating of the laser beams.

## 4.3 Birefringence measurements

We have already discussed the single channel map that we obtain by measuring a projection of the probe (figure 4.1a). Since we are interested in the different behaviour of the two projections, we build a birefringence map (third panel in figure 4.4) by subtracting the Ch1 map from the Ch0 map. The data provided by these birefringence maps will be compared with the equation 2.14 (first order) and the equations 2.17 and 2.18 (third order), derived in the second chapter. For this reason, the upcoming data analysis will be focused on the birefringence maps only.

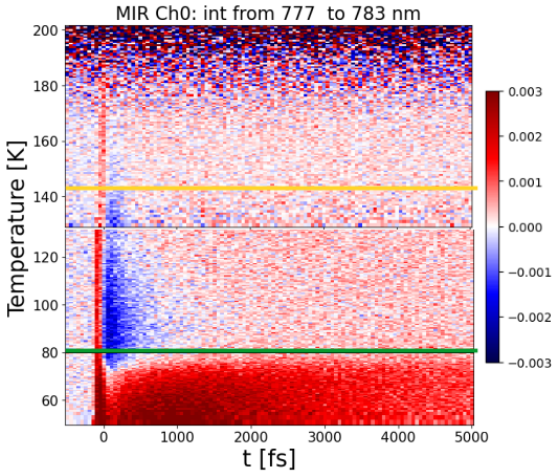


(a) $T_C$ (green line) and $T^*$ (yellow line) for the OP sample.

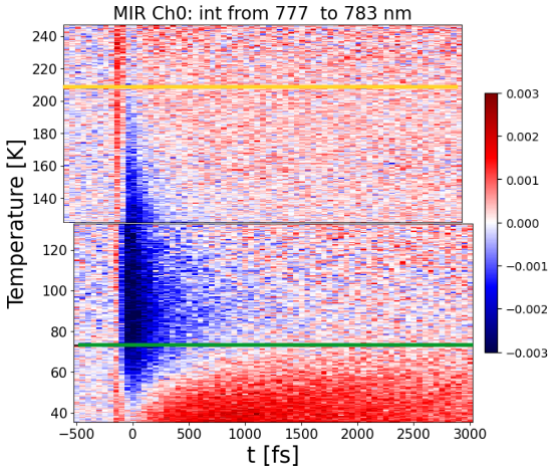


(b) $T_C$ (green line) and $T^*$ (yellow line) for the UD sample.

Figure 4.2

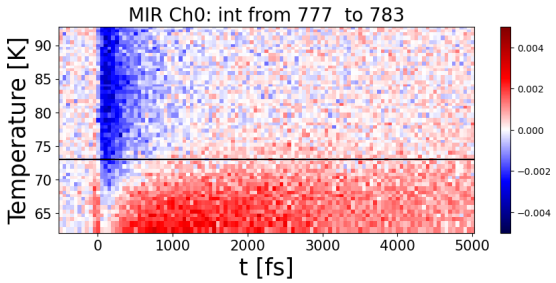


(a) Temperature scan with a repetition rate of 5kHz.

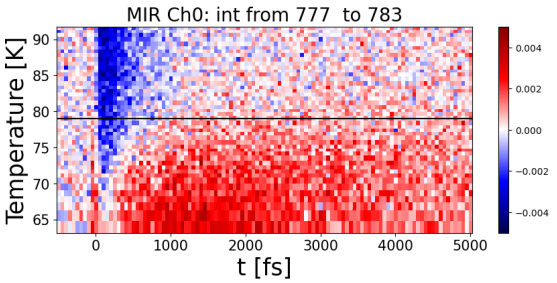


(b) Temperature scan with a repetition rate of 2kHz.

Figure 4.3: Effect of the repetition rate of the laser on the critical temperature $T_C$ in the UD sample.

The reflectivity maps depend on the reflectivity intensity, the wavelength of the reflected probe and the time-delay between the pump and the probe. In order to compare them with the model given in the second chapter, that depends only on the intensity, we must integrate the data of the birefringent maps over an appropriate region (third map in figure 4.4). We identify the wavelength range considering the region in which there is signal, ignoring the contributions near the edge where there is noise because of the low intensity of the probe beam impinging on the edges of the arrays. On the time axis we consider the interval that goes from the time in which the pump excites the sample (t=0) to the time in which the signal starts to lose intensity. We have done this choice for every map in the following analysis.

### 4.3.1 Error analysis

To compute the errors on the wavelength axis we consider the "negative" time (when the sample is in equilibrium) in the single channel maps and we calculate the variance with respect to zero for each wavelength. Then we obtained the variance for the birefringence map for each wavelength through the sum of the errors obtained for the single channels. The errors for each instant on the time axis are equal: we calculate the variance propagation

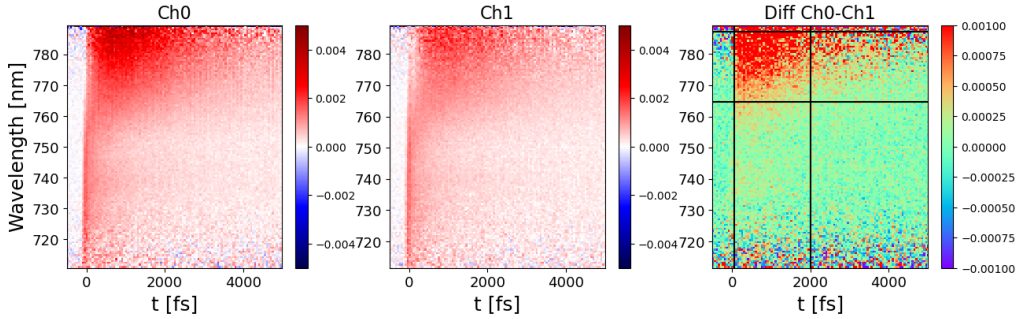


Figure 4.4: **Birefringence map**: The first and second maps correspond to the reflectivity signal $\Delta R/R$ collected by the two detectors. The third figure is obtained subtracting the second from the first.

considering the average of the different wavelength contributions:

$$\sigma_t = \frac{\sqrt{\sum_i \sigma_i^2}}{n}, \tag{4.1}$$

where $\sigma_i^2$ are the birefringence variances calculated for the $n$ wavelength contributions. Then we average along the time axis (for m points) obtaining the final error for the map:

$$\sigma_{map} = \frac{\sigma_t}{\sqrt{m}}. \tag{4.2}$$

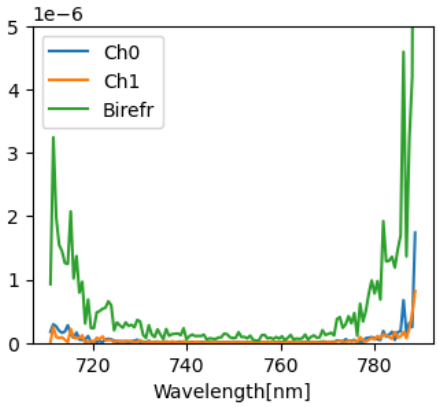


Figure 4.5: **Variances in function of the wavelength**: The blue and orange lines are the variances calculated with respect to zero for the single channels, considering the "negative" time, when the sample is in equilibrium. The green line is the variance for the Birefrangent signal.

### 4.3.2 Comparison between SC, PG and Normal phase

In order to study the dependence of the birefringent signal on the temperature, we perform the same measurement of figure 4.4 also in pseudogap and normal phases. The measurements presented in figure 4.6 are done in the underdoped sample, with the pump polarization parallel to the CuO axis. In fact in the superconducting (SC) phase we obtained a positive signal in the region of high wavelengths (760nm-790nm). The signal decreases starting from 2ps. In pseudogap (PG) phase we have only a short negative signal for high wavelengths and a weaker positive signal for lower wavelengths at the overlap. In normal (N) phase there is not signal, except for a weak positive signal at the overlap. So from the figure it is clear that the signal that we obtained is peculiar of the superconducting phase.

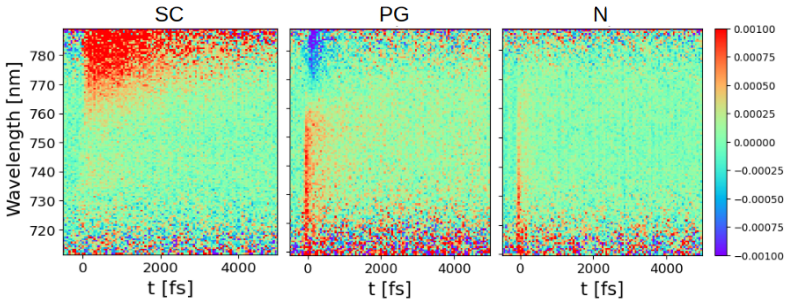


Figure 4.6: **Comparison of the birefringence maps in the SC, PG and normal phase.** Birefringence maps obtained in the underdoped sample with the pump polarization parallel to the CuO bond, measured at 35K (left), 98.5K (centre) and 295K (right).

### 4.3.3 Dependence from probe angle

In order to study the relaxation of the sample along the different axes of the sample we rotate the polarization of the incoming probe ($\phi$) and the reflected probe ($\alpha$) through two half waveplates. We study the dependence from the probe angle for both the polarization of the pump. The first half waveplate is placed before the sample and it is rotated by step of 22.5°. The second one (analyzer) is placed after the sample and before the polarizing beam splitter. We use it to realign the reflected beam with the polarization of the incoming probe.

Figure 4.7 represents a set of measurements done rotating the probe polarization over a range of 360° in the underdoped sample. The polarization angles ($\phi$) are reported above each map (0° means that the probe is parallel to the CuO bond). In this case the pump is parallel to the CuO bond, the wavelength is 17$\mu$m and the power is 0.3mW. The measurements are done in the superconducting phase, at $T = 50K$. There are maximum signals for probe angles $\phi = k\pi/2$. The positive and negative signals have same characteristics: they both have wavelengths in the range 760-780nm and duration of 2ps. For the others probe angles there are null signals. Therefore there is a is periodicity of 180° in the measurements.

This periodicity can be seen also performing a polar plot of the birefringent maps (figure 4.8. We averaged the data of the maps as described in section 4.3 and we plotted the absolute values of the signals in polar coordinates. From this plot is clear that the positive signal and the negative signal are symmetric also in amplitude.

Therefore is sufficient study the sample for probe angles in the interval $(0°, 180°)$. In the next chapter we analyze the data collected in the different configurations always considering this range of angles.

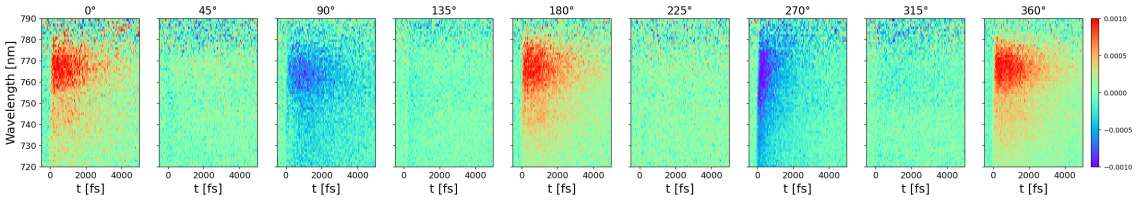


Figure 4.7: **Birefringence maps for different probe polarizations.** The measurments are done in the underdoped sample at a temperature of 50K. The pump polarization is along the CuCu axis.

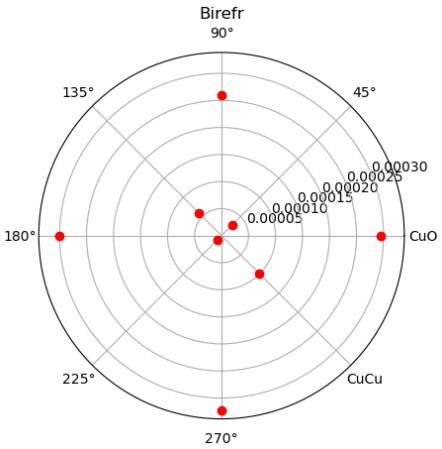


Figure 4.8: **Polar representation of the birefringence maps.** To plot this figure we average the data in the region described in section 4.3 and then plot their absolute values in polar coordinates.

## 4.4 Measurements in SC phase: comparison with the models

In this section we present the measurements done in SC phase exciting the two samples with a pump of energy lower than the gap energy ($\lambda = 17\mu m$). Then we present a comparison between the data collected and the theoretical model developed in the second chapter. The main comparison is between the two configurations of the pump polarization: for the pump parallel to the CuO axis ($\theta = 0°$) and for the pump parallel to the CuCu axis ($\theta = 45°$)

### 4.4.1 Underdoped sample

In figure 4.9a there are the reflectivity maps of the measurements done on the UD sample with the pump polarization along the CuCu bond ($\theta = 45°$). The amplitude of the signal is maximum when the probe is parallel to the CuO bond ($\phi = k\pi/2$) and is zero when the probe is along the CuCu bond ($\phi = k\pi/4$).

In figure 4.9b there is a comparison between the different phases. In PG and normal phases there are weak signals for all the probe angles that can be explained as noise or effects connected to the specific phases. We do not know if and how these signals affect the measurements in the superconducting phase. For this reason we will consider only the SC data not contained in the region highlighted in grey. Thank to this observation, in 4.9c (where the dashed grey lines individuate the CuO axis) we see that the measurements agree with the third order tensor model (represented with dashed orange line, $B_{2g}$ mode in this case). Instead the first order tensor model is not respected because null signals are not predicted. So the zero birefringence signal suggests that the pump polarization is a necessary parameter to describe the selection rules in a pump and probe experiment.

The maps in figure 4.10a represented the measurements collected with the pump polarization rotated of 45° (parallel to CuO bond). We have maximum signal along the CuO bond, like the previous case in which the pump is parallel to CuCu bond. Furthermore we have weaker positive signal also for $\phi = 45°$ and there is not a symmetric negative signal for $\phi = 135°$, where there is a null signal. For the consideration done in the previous paragraph about the signals in PG and normal phases, this weaker positive signal can not be considered zero, in fact it is not contained in the grey region (figure 4.10b).

From the third order model we expect maximum signal for probe angles $\phi = k\pi/4$ and

null signal for $\phi = k\pi/2$, but we have signals at three over four probe angles. In this configuration, the first order model, that does not predict zeros, seems to be more descriptive of the experiment. But we have a null signal for $\phi = 135°$. So in this configuration neither of the models can explain the behaviour of the sample excited along the CuO axis.

### 4.4.2 Optimally doped sample

We consider now the same two configurations but on the optimally doped sample.

In the case of the pump polarization along the CuCu axis (figure 4.11a), we have maximum signal at probe angles $\phi = 0°, 90°$ and null signal for $\phi = 135°$. In the second birefringence map there is a clear positive signal weaker than the maximum signal for $\phi = 0°$, that can not be explained as noise considering the comparison map 4.11b. The third order model does not consider the doping as a parameter. So the prediction for the optimally doped sample is equal to the result for the underdoped sample seen before. So the third order model can explain the maximum signals and the null signal, but does not explain the positive signal for $\phi = 45°$. Analogously considerations are done for the first order model: it predicts signals for all probe angles, but we have signals for only three angles. Also for this configuration neither the third or first order models are respected.

In the case of the pump along the CuO axis (figure 4.12a) analogously to the UD sample, there are maximum signals for probe angles $\phi = 0°, 90°$ and null signals for $\phi = 45°, 135°$. The third order model predicts maximum signals where we have null signals and vice versa. We have signals for two angles over four, so neither the first order model is respected. Also in this configuration both models can not describe the measurements obtained.

### 4.4.3 Discussion

In the second chapter we developed two models for the Raman tensor: the first order model that considers only the action of probe beam and the third order model, implemented to study time-resolved measurements, in which the action of the pump is considered. In their derivation, we considered the symmetry properties of the material; in particular we used two electronic symmetries: $B_{1g}$ and $B_{2g}$ modes, that probe respectively the antinodal and nodal regions of the first Brillouin zone. The first order model predicts signals at each probe angle $\phi$: it is proportional to $B_{2g}$ for $\phi = k\pi/2$ and to $B_{1g}$ for $\phi = \pi/4 + k\pi/2$, where for $\phi = 0°$ the polarization is considered parallel to the CuO axis. The third order model predicts instead different behaviour as function of the pump polarization. If the pump polarization is parallel to the CuO bond, the $B_{1g}$ mode is isolated; the model predicts signal along the CuCu axis and null signal along the CuO axis. If the pump is parallel to the CuCu bond, the $B_{2g}$ mode is instead isolated; the model predicts signal along the CuO axis and null signal along the CuCu axis.

Considering the measurements described in the previous sections and comparing them with the models, we can make some observations for the measurements done in the superconducting phase:

- the birefringent signal is restricted for high wavelengths, in the range 760nm-790nm;

- the third order tensor model well describes the selection rules of cuprates only for the UD sample in the configuration in which the pump polarization is along the CuCu axis. The model predicts correctly maximum signals along the CuO axis and null signals along the CuCu axis;

- for the OP sample there is a weak positive signal for $\phi = 45°$ when the pump is along the CuCu axis. This signal is not in agreement with the predictions of the third order model;
- if the pump is parallel to the CuO axis we obtained the maximum (and the null) signals shifted of 45° with respect to the prediction of the third order tensor model for both the samples;
- the first order model is never respected because it does not predict null signals. In fact in all the configurations obtained varying the pump polarization and the doping of the sample we have null signals.

From these observations we can conclude that neither the models developed describe the selection rules of our samples.

Nonetheless, the signals that we measured are certainly peculiar of the superconducting phase because performing the same measurements at different temperatures the data collected do not depend on the probe angles. Therefore, we can conclude that cuprates have a birefringent behaviour only below the critical temperature.

Figure 4.9: Pump // CuCu, UD sample

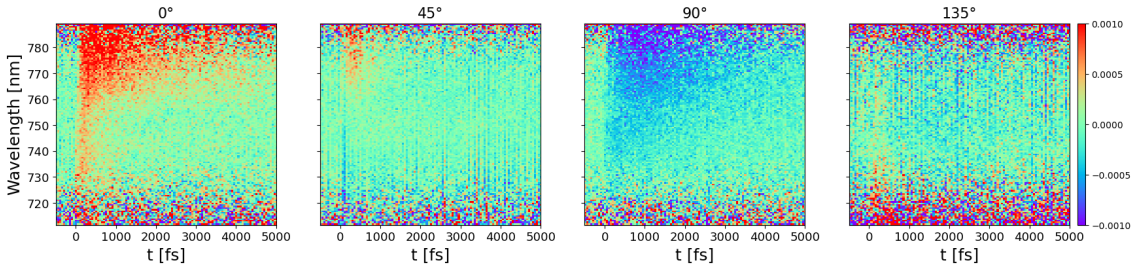


(a) Reflectivity map

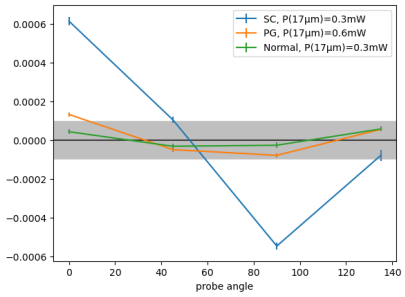


(b) Comparison with the pseudogap and normal phases.

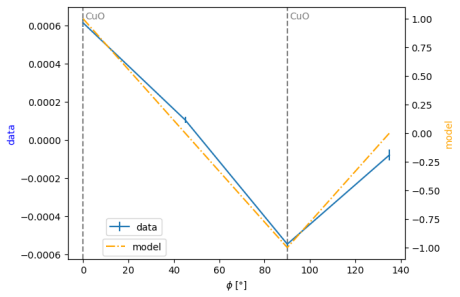


(c) Comparison with the third order theoretical model ($B_{2g}$ mode)

Figure 4.10: Pump // CuO, UD sample

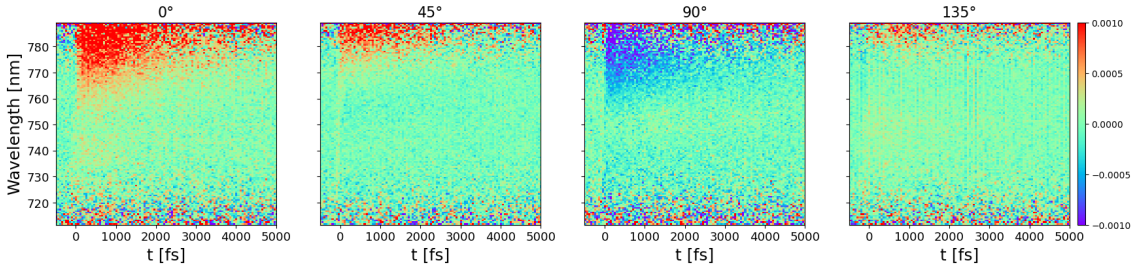


(a) Reflectivity map

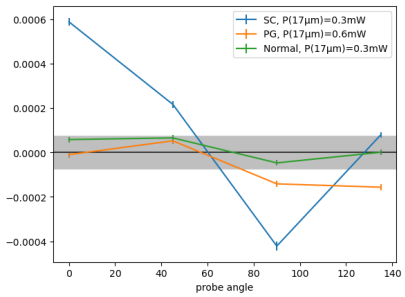


(b) Comparison with the pseudogap and normal phases.

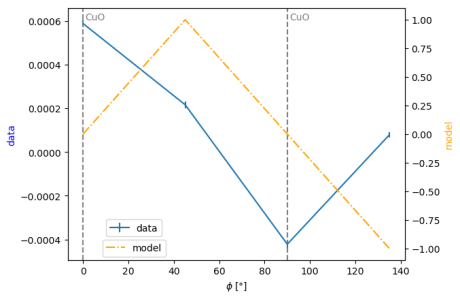


(c) Comparison with the third order theoretical model ($B_{1g}$ mode)

Figure 4.11: Pump // CuCu, OP sample

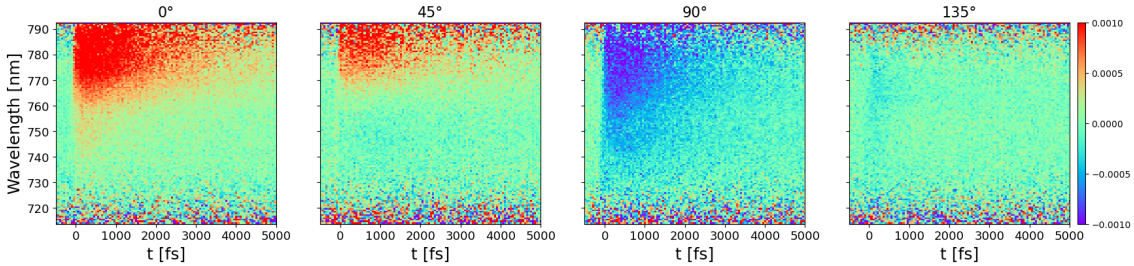


(a) Reflectivity map

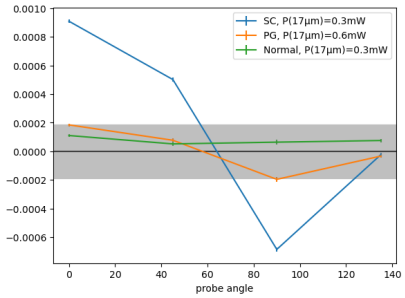


(b) Comparison with the pseudogap and normal phases.

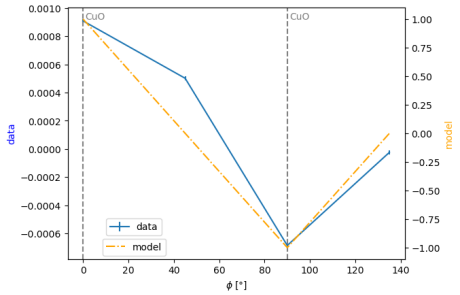


(c) Comparison with the third order theoretical model ($B_{2g}$ mode)

Figure 4.12: Pump // CuO, OP sample.

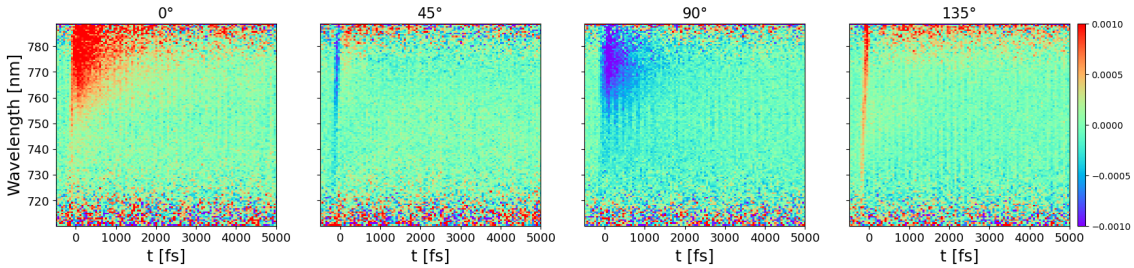


(a) Reflectivity map

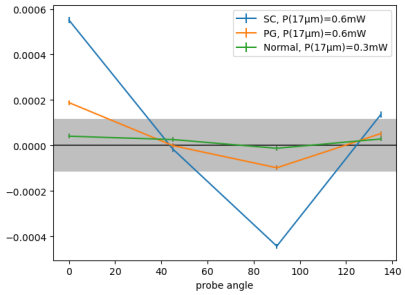


(b) Comparison with the pseudogap and normal phases.

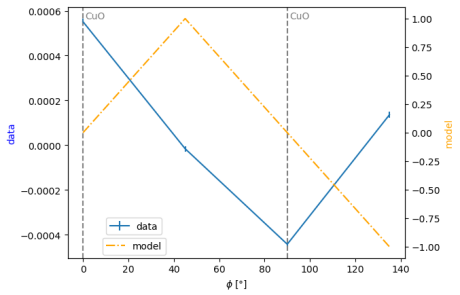


(c) Comparison with the third order theoretical model ($B_{1g}$ mode)

# Conclusions

In this thesis, we focused on an optimally doped and an underdoped sample of the cuprate $Bi_2Sr_2CaCu_2O_{8+\delta}$. This system is a high temperature superconductor that displays a superconducting gap with d-wave symmetry. The anisotropic gap defines two axes in the momentum space: along the nodal direction the gap has maximum value, along the antinodal it vanishes.

By implementing electronic Raman scattering measurements in a time-resolved pump-probe scheme, we measured the samples in different regions of the phase diagrams and studied the Raman-like optical response in different polarization configurations.

In order to interpret the results, we developed a third-order model for the Raman tensor that, in addition to the standard dependence on the probe polarization, also takes into account the polarization of the pump. We used this model, together with the first order model, that does not involve the action of the pump, to study the birefringent data collected during the measurements at superconducting temperature.

In order to understand if the data collected are characteristic of the superconducting phase, we performed the measurements also at higher temperature, in pseudogap and normal phase. In pseudogap phase and normal phase we obtained null or weak signals for all the probe angles, that can be ascribed to noise or to weak effects connected to the specific phase. Instead, we obtained clear birefringent signals only below the critical temperature, so directly related to the superconducting phase.

The measurements disagree with both models developed. In fact in none of the configurations (varying pump and sample) we found a birefringent signal regardless of the probe polarization angle. This means that the first order model is in contrast with the measurements. Instead, the third order tensor model well describes the selection rules only for the UD sample in the configuration in which the pump polarization is along the CuCu axis. If the pump polarization is parallel to the CuO axis, we obtained maximum signals shifted of 45° with respect to the third order model prediction.

In two configurations (UD-pump//CuO and OP-pump//CuCu) there is a weak positive signal for $\phi = 45°$, but there is not a symmetric negative signal for $\phi = 135°$. This result suggests that there might be a breaking of the $D_{4h}$ symmetry because of the action of the pump. In fact the $D_{4h}$ is characterized by a 90° symmetry, but some of the birefringent signals that we collected have a 180° periodicity. Previous studies [9] had proved that in cuprates there is a 90° symmetry breaking, in favor of a 180° symmetry like the $D_{2h}$. In order to test this option we should write the third order Raman tensor also considering the modes selected by this symmetry and compare the data collected also with its predictions.

Furthermore, to perform these measurements, we used a pump pulse with an energy lower than the gap energy and probe pulses of wavelengths in the range of 720-790nm. To learn more about the symmetry of cuprates and how they respond to photoexcitation, it might be interesting to perform similar measurements also with pump pulses with higher photon energy and with probe pulses having a broader spectral content, possibly covering higher wavelengths where the birefringent signal seems to be more intense.

Finally, also changing the doping of the sample might be useful to study the behaviour

of these materials across the entire phase diagram.

# Bibliography


[1] Thomas P Devereaux and Rudi Hackl, *Inelastic light scattering from correlated electrons.* Reviews of modern physics, 2007.

[2] Angela Montanaro, *Non-equilibirum response of quantum materials to resonant low-energy electronic photo-excitations*, PhD thesis, 2022.

[3] Claudio Giannetti, Massimo Capone, Daniele Fausti, Michele Fabrizio, Fulvio Parmigiani, Dragan Mihailovic, *Ultrafast optical spectroscopy of strongly correlated materials and high-temperature superconductors: a non-equilibrium approach*, Advances in Physics, 2016.

[4] C. Kittel, *Introduction to Solid State Physics*, John Wiley & Sons Inc, 8th edition.

[5] Neil W. Ashcroft, N. David Mermi, *Solid state physiscs*, Harcourt College Publishers, 1976.

[6] P. Coleman, *Introduction to Many Body Physics*, Cambridge University Press, 2015.

[7] C. Thomsen and G. Kaczmarczyk, *Vibrational raman spectroscopy of high-temperature superconductors*, 2002.

[8] F. Cilento, *Non-equilibrium phase diagram of $Bi_2Sr_2Y_{0.08}Ca_{0.92}Cu_2O_{8+\delta}$ cuprate superconductors revealed by ultrafast optical spectroscopy*, PhD thesis, 2010.

[9] Hamidian M, Edkins S, Joo SH, Kostin A, Eisaki H, et al. 2016. Nature 532:343–47.